Inorganic Chemistry

Article

Cite This: Inorg. Chem. 2017, 56, 14315-14325

pubs.acs.org/IC

Ligand Substituent Effects in Manganese Pyridinophane Complexes: Implications for Oxygen-Evolving Catalysis

Song Xu,[†] Lukas Bucinsky,[‡] Martin Breza,[‡] J. Krzystek,[§] Chun-Hsing Chen,[†] Maren Pink,[†] Joshua Telser,[▽] and Jeremy M. Smith*[,†]

[†]Department of Chemistry, Indiana University, Bloomington, Indiana 47405-7102, United States

[‡]Institute of Physical Chemistry and Chemical Physics, Faculty of Chemical and Food Technology, Slovak University of Technology, Radlinského 9, SK-81237 Bratislava, Slovakia

[§]National High Magnetic Field Laboratory, Florida State University, Tallahassee, Florida 32310, United States

[▽]Department of Biological, Chemical and Physical Sciences, Roosevelt University, Chicago, Illinois 60605, United States

Supporting Information

ABSTRACT: A series of Mn(II) complexes of differently substituted pyridinophane ligands, $(Py_2NR_2)MnCl_2$ (R = ^{i}Pr, Cy) and $[(Py_2NR_2)MnF_2](PF_6)$ (R = ^{i}Pr, Cy, ^{t}Bu) are synthesized and characterized. The electrochemical properties of these complexes are investigated by cyclic voltammetry, along with those of previously reported $(Py_2NMe_2)MnCl_2$ and the Mn(III) complex $[(Py_2NMe_2)MnF_2](PF_6)$. The electronic structure of this and other Mn(III) complexes is probed experimentally and theoretically, via high-frequency and -field electron paramagnetic resonance (HFEPR) spectroscopy ab initio quantum chemical theory (QCT), respectively. These studies show that the complexes contain relatively typical six-coordinate Mn(III). The catalytic activity of these complexes toward both H_2O_2 disproportionation and H_2O oxidation has also been investigated. The rate of H_2O_2 disproportionation decreases with increasing substituent size. Some of these complexes are active for electrocatalytic H_2O oxidation; however this activity cannot be rationalized in terms of simple electronic or steric effects.

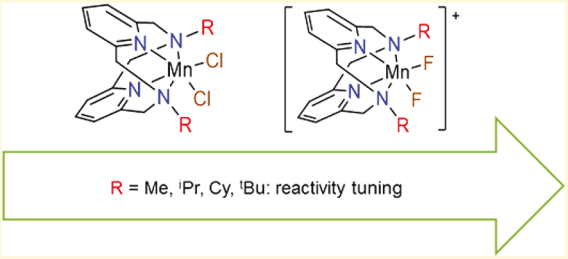

INTRODUCTION

An attractive strategy for meeting the dramatically increasing demand of clean and renewable energy is to use hydrogen gas as the energy source, which can be obtained from the splitting of H_2O to H_2 and O_2.[1−3] H_2O is split by Nature under mild conditions, using natural oxygenic photosynthesis, which is achieved via the Oxygen Evolving Center (OEC) of Photosystem II. The active site of OEC has been characterized as a Mn_4Ca cluster through spectroscopic, X-ray diffraction (XRD), and computational studies.[4−7] Mechanistic investigations suggest that the product O−O bond is formed at higher manganese oxidation states, which are accessed via a series of proton-coupled electron transfer steps, but detailed information on/about the structure and electron configuration of the transient state in which O−O coupling occurs is still lacking.[5]

To better understand this natural H_2O splitting process, numerous functional and structural model complexes have been synthesized and investigated.[1,8] Because of Mn being at the active site of the OEC, Mn-based water oxidizing complexes are of particular interest.[5] While several biomimetic/bioinspired dinuclear and multinuclear Mn water oxidation catalysts have been reported, mononuclear manganese catalysts for water oxidation catalyst are rare.[8] As well as being more synthetically accessible, mononuclear complexes have the potential for relatively straightforward delineation of structure/activity relationships on water oxidation reactivity. Previously, our group reported one such complex: $(Py_2N^tBu)_2MnBr_2$ (where $Py_2N^tBu_2$ is the *N,N′*-di-*tert*-butyl-2,11-diaza[3,3](2,6)-pyridinophane ligand), which catalyzes H_2O oxidation to O_2 at ca. −1.5 V vs NHE. Since control experiments did not find evidence for the formation of nanoparticulate or heterogeneous catalysts, water oxidation catalysis is likely homogeneous in nature.[9] Interestingly, replacing the *tert*-butyl ligand substituent in $(Py_2N^tBu)_2MnBr_2$ with hydrogen or methyl groups, respectively, to give $(Py_2NH_2)MnBr_2$ and $(Py_2NMe_2)MnBr_2$, results in a loss of water oxidation activity; however, these complexes were found to catalyze H_2O_2 disproportionation to H_2O and O_2.[9,10] Therefore, the latter complexes are functional models of the nonheme type II, Mn-containing catalases (Mn-CAT), which perform this reaction in a broad range of microorganisms.[11]

In addition to H_2O oxidation and H_2O_2 disproportionation, the Py_2NR_2 ligand framework has been shown to support metal complexes that catalyze a variety of other reactions. For example, Koch showed early on that Fe^{III}/Py_2NMe_2 catalyzes the oxidative degradation of catechols by O_2.[12,13] More recently, Mirica reported carbon−carbon and carbon−hetero-

Received: September 22, 2017
Published: November 8, 2017

DOI: 10.1021/acs.inorgchem.7b02421
Inorg. Chem. 2017, 56, 14315−14325

atom bond formation catalyzed by $Ni^{III}/Py_2N^tBu_2$.[14] In addition to catalysis, spin crossover was also observed for a $Fe^{II}/Py_2N^tBu_2$ complex.[15] The ability to modify the R groups of Py_2NR_2 ligands allows the catalytic behavior of their metal complexes to be tuned. For example, Cho reported that aldehyde deformylation catalyzed by Ni^{III}/Py_2NR_2 can be significantly accelerated when switching from R = *tert*-butyl to cyclohexyl, which they attributed to a reduction in bulkiness.[16] Since we previously demonstrated that the catalytic reactivity of Mn/Py_2NR_2 toward O_2 evolution is influenced by the pyridinophane ligand substituent, we became interested in systematically delineating the relationship between the pyridinophane ligand substituents and the reactivity of their manganese complexes.

Here, we report the synthesis and structural characterization of $(Py_2NR_2)MnCl_2$ (R = ^{i}Pr (**2**), Cy (**3**)) and $[(Py_2NR_2)MnF_2](PF_6)$ (R = ^{i}Pr (**6**), Cy (**7**), ^{t}Bu (**8**)) complexes (Scheme 1). Along with structural, electrochemical, and catalytic

Scheme 1. $(Py_2NR_2)MnCl_2$, $[(Py_2NR_2)Mn(NCMe)_2]^{2+}$, and $[(Py_2NR_2)MnCl_2]^+$ Complexes in This Work

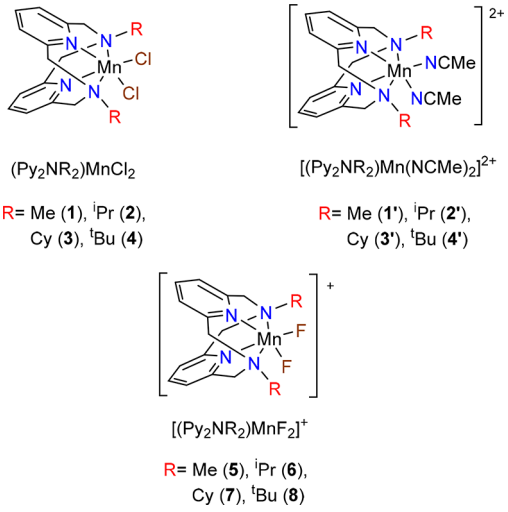

properties of previously reported $(Py_2NMe_2)MnCl_2$ (**1**), $[(Py_2NMe_2)MnF_2]^+$ (**5**) complexes,[17] we have investigated the effect of the *N*-substituents on the catalytic reactivity of these complexes toward H_2O_2 disproportionation and H_2O oxidation.

We have also elucidated the electronic structure of these complexes through a combination of experiment and theory, primarily high-frequency and -field electron paramagnetic resonance (HFEPR) spectroscopy and quantum chemical theory (QCT) calculations. While density functional theory (DFT) calculations on $[(Py_2NMe_2)MnF_2](PF_6)$ (**5**) were reported by Albela et al.,[17] herein, a multiconfigurational treatment allows for a more accurate assessment of the electronic structure description and zero-field splitting (ZFS).[18,19] Therefore, we used the complete active space self-consistent field (CASSCF) method[18,20−22] (treating spin−orbit coupling (SOC) effects perturbatively[23]) to investigate the electronic structure of $[(Py_2NR_2)MnX_2]^+$ (X = F^-, Cl^-), including *n*-electron valence (electron) second-order perturbation theory (NEVPT2)[24−26] to account for dynamic electron correlation effects and multireference configuration interaction (MRCI)[18,20,27] to assess the spin−spin contribution, as well as DFT level for completeness. These results provide an experimental calibration for a similar computational investigation of the hydroxido complex, $[(Py_2N^tBu_2)Mn(OH)_2]^+$ which has been proposed as an intermediate in electrocatalytic water oxidation by a Mn pyridinophane complex.[28,29]

RESULTS AND DISCUSSION

Preparation and Characterization of $(Py_2NR_2)MnCl_2$ and $[(Py_2NR_2)MnF_2]^+$ (R = Me, ^{i}Pr, Cy, ^{t}Bu). Similar to the previously reported bromide analogues, $(Py_2NR_2)MnBr_2$ (R = H, Me, ^{t}Bu),[9,10] complexes **1**−**4** were prepared by treating the appropriate Py_2NR_2 ligand with anhydrous $MnCl_2$ in acetonitrile solution (see Scheme 2a). The pale yellow

Scheme 2. Synthesis of the (a) $Py_2NR_2MnCl_2$ and (b) $[Py_2NR_2MnF_2](PF_6)$ Complexes

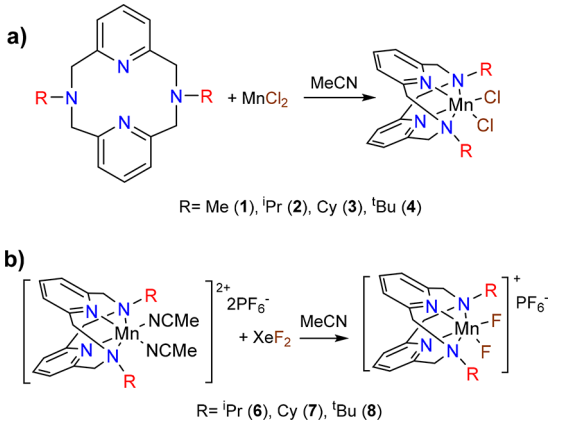

$(Py_2NR_2)MnCl_2$ products were characterized by single-crystal X-ray diffraction (XRD) and high-resolution mass spectrometry (HRMS). Complex **2** can be converted to the acetonitrile-solvated complex, **2′**, by treating **2** with 2 equiv of $TlPF_6$ in acetonitrile solution, as previously reported for **1′** and **4′**.[9,10] Complex **2′** has also been characterized by single-crystal XRD.

The Mn(III) difluoride complex **6** can be prepared in an analogous manner to the synthesis of **5**,[17] wherein a mixture of $Py_2N^iPr_2$ and MnF_3 is gently heated in MeOH. Unfortunately, this protocol does not work for the synthesis of complexes **7** and **8**, presumably because of the poor methanol solubility of the ligands, with their bulky aliphatic substituents. However, these complexes can be obtained via the fluorination of **3′** and **4′** with XeF_2 in MeCN, similar to the preparation of other organometallic fluoride complexes.[30,31] Complex **6** can also be prepared by this method. Complexes **6**, **7**, and **8** were isolated as dark orange crystals and characterized by single-crystal XRD and HRMS. Note that XeF_2 is typically a two-electron oxidant that transfers two F atoms to the metal;[31] however, only the one-electron oxidized products (**6**, **7**, and **8**) were obtained from these fluorination reactions (see Scheme 2b). We therefore propose that the Mn(III) complexes (**6**, **7**, **8**) are generated through comproportionation of the two-electron oxidized Mn(IV) complexes $[(Py_2NR_2)MnF_2]^{2+}$ (formed by two-electron oxidation by XeF_2) and the Mn(II) reagents, $[(Py_2NR_2)Mn(NCMe)_2]^{2+}$.

The ultraviolet−visible light (UV-vis) absorption spectra of complexes **6**−**8** each show a band at ∼500 nm that has a low extinction coefficient (Figures S4−S6 in the Supporting Information), similar to the observations for **5**.[17] The high spin state of Mn(III) ($3d^4$, $S = 2$) is confirmed by the magnetic susceptibility of **8** (μ_{eff} = 5.20 μ_B, as determined via the Evans

DOI: 10.1021/acs.inorgchem.7b02421
Inorg. Chem. 2017, 56, 14315−14325

method), which is consistent with the theoretical value calculated for $S = 2$ ($\mu_{eff} = 4.90\ \mu_B$).

Molecular Structures of $[(Py_2NR_2)Mn(NCMe)_2]^{2+}$ and $[(Py_2NR_2)MnF_2]^+$ (R = Me, ^{i}Pr, Cy, ^{t}Bu). X-ray quality crystals of **1′**, **2′**, **4′**, **3**, **6**, **7**, and **8** were obtained by slow diffusion of diethyl ether into concentrated acetonitrile solution at ambient temperature. Representations of the molecular structures are shown in Figures 1 and 2, with selected bond distances and angles given in Tables 1 and 2. We were unable to isolate crystals of **3′** suitable for X-ray diffraction (XRD) studies, although its chloride analogue (**3**) was successfully characterized by single-crystal XRD, providing data for comparison with the acetonitrile complexes (**1′**, **2′**, and **4′**).

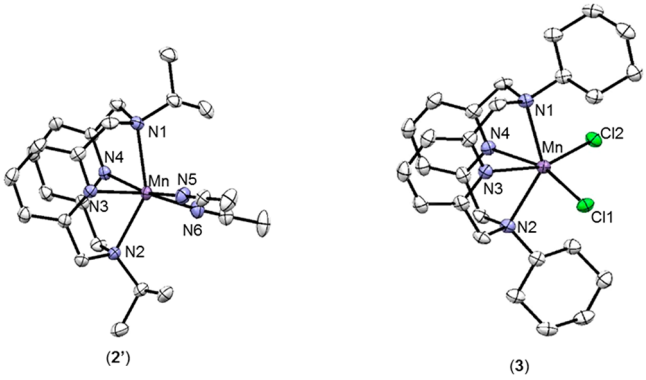

Figure 1. ORTEPs of complexes **2′** and **3** (50% ellipsoids; hydrogen atoms and PF_6 anions are omitted for the sake of clarity). Selected bond lengths for **3**: Mn−N1, 2.444(2); Mn−N2, 2.444(2) Å; Mn−N3, 2.273(2) Å; Mn−N4, 2.273(2) Å; Mn−Cl1, 2.4350(8) Å; and Mn−Cl2, 2.4350(8) Å. Selected bond angles for **3**: N1−Mn−N2, 138.42(2)°; N3−Mn−N4, 72.84(13)°; and Cl1−Mn−Cl2, 104.54°.

According to the structural data summarized in Table 1, the structures of the Mn(II) complexes, **1′**, **2′**, and **4′** are generally similar to the previous reported analogues (**1**) and the bromide series $(Py_2NR_2)MnBr_2$ (R = Me, ^{t}Bu).[9,10,17] Specifically, these mononuclear complexes all exhibit pseudo-octahedral geometries with an equatorial plane consisting of two acetonitrile ligands and two pyridine donors, with the amines occupying the axial positions. The geometry of the pyridinophane ligand ensures that the acetonitrile (or other ancillary) ligands are *cis* with respect to each other and *trans* to the pyridine donors.

Table 1. Selected Bond Lengths and Angles of 1′, 2′, and 4′

	$[Py_2NR_2Mn^{II}(NCMe)_2]^{2+}$		
	Me (**1′**)[a]	^{i}Pr (**2′**)	^{t}Bu (**4′**)[b]
Bond Lengths (Å)			
Mn−N1	2.327(2)	2.357(1)	2.455(2)
Mn−N2	2.328(2)	2.365(2)	2.415(2)
Mn−N3	2.198(2)	2.198(1)	2.236(2)
Mn−N4	2.213(2)	2.216(1)	2.165(2)
Mn−N5	2.174(2)	2.191(1)	2.152(2)
Mn−N6	2.184(2)	2.208(2)	2.210(2)
Bond Angles (deg)			
N1−Mn−N2	143.44(6)	143.52(5)	143.41(6)
N3−Mn−N4	77.61(6)	77.58(4)	75.10(7)
N5−Mn−N6	94.54(7)	90.74(5)	96.91(8)

[a]Data taken from ref 10. [b]Data taken from ref 9.

Complex **3** has a similar structure to that of **1′**, **2′**, **4′**, although the N(amine)−Mn−N(amine) and N(pyridine)−Mn−N(pyridine) bond angles are significantly smaller for **3**, likely a consequence of the larger chlorido ligands. This response to the change in ancillary ligands suggests the pyridinophane ligand has flexibility in its binding mode. In this context, note that similar bond angles involving the pyridinophane ligand are observed for **1**[17] and **3**, both of which contain chlorido ligands.

The data in Table 1 show that the pyridinophane substituents have a significant effect on the Mn-amine distances in the $[(Py_2NR_2)Mn(NCMe)_2]^{2+}$ complexes. For example, the Mn−N(amine) distance in **4′** is 0.103 Å longer than the corresponding distance in **1′**. By contrast, the complexes show no significant difference in Mn−N(pyridine) and Mn−N(acetonitrile) distances. Assuming that the chlorido ligands in **3** do not significantly perturb the other bond lengths, the combined data suggests that the Mn−N(amine) distance increases as the bulkiness of the pyridinophane substituent increases.

The Mn(III) complexes **6**−**8** are generally similar in structure to those of the Mn(II) complexes discussed above. Thus, the Mn ions are also coordinated by the tetradentate macrocycle and two fluorido ligands that are *cis* with respect to other (Figure 2). However, the Mn(III) complexes generally have shorter bond lengths, which is attributed to the smaller size of the Mn(III) ion (Table 2). Similarly to **5**,[17] **6**−**8** also show characteristic Jahn−Teller elongations along the axis

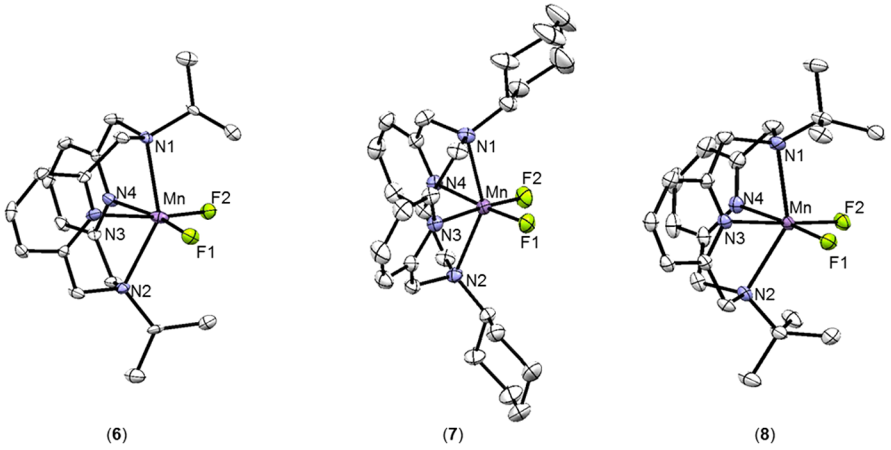

Figure 2. ORTEPs of complexes **6**, **7**, and **8** (50% ellipsoids; hydrogen atoms and PF_6 anions are omitted for the sake of clarity).

DOI: 10.1021/acs.inorgchem.7b02421
Inorg. Chem. 2017, 56, 14315−14325

Table 2. Selected Bond Lengths and Angles of 5, 6, 7, and 8

	$[Py_2NR_2Mn^{III}F_2]^+$			
	Me (**5**)[17]	^{i}Pr (**6**)	Cy (**7**)	^{t}Bu (**8**)
Bond Lengths (Å)				
Mn−N1	2.274(2)	2.328(4)	2.314(2)	2.337(1)
Mn−N2	2.278(2)	2.328(4)	2.310(2)	2.332(2)
Mn−N3	2.024(2)	2.089(3)	2.002(2)	2.018(2)
Mn−N4	2.020(2)	2.089(3)	2.009(2)	2.008(1)
Mn−F1	1.805(2)	1.754(3)	1.806(2)	1.805(1)
Mn−F2	1.801(2)	1.754(3)	1.811(1)	1.810(1)
Bond Angles (deg)				
N1−Mn−N2	147.03(8)	145.3(2)	145.14(8)	145.37(5)
N3−Mn−N4	77.07(8)	79.61(8)	86.76(8)	85.72(6)
F1−Mn−F2	94.89(8)	100.58(7)	92.94(7)	95.77(5)

containing the amine donors, as revealed by Mn−N(amine) bond lengths that are significantly longer (ca. 0.3 Å) than the Mn−N(pyridine) distances. Interestingly, the Mn−N(amine) distances for **5** are significantly shorter than those observed for **6**−**8**, which are similar in magnitude, suggesting that this distance is not strongly dependent on the size of the substituent, in contrast to the Mn(II) complexes.

High-Frequency and -Field EPR. Given that Mn(III) complexes generally are highly amenable to study by HFEPR,[32−35] and the pyridinophane complex $[(Py_2NMe_2)MnF_2](PF_6)$ (**5**) in particular had been previously investigated experimentally by HFEPR, as well as computationally, by Albela et al.,[17] we decided to confirm and extend those studies. HFEPR investigation of **6** was most successful and clearly showed the $S = 2$ ground state, with a negative D value, as seen in the HFEPR spectrum and simulations shown in Figure 3.

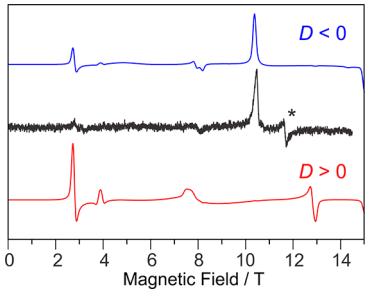

Figure 3. A 633.6 GHz, 5 K HFEPR spectrum of **6** as a pellet (black trace) with two simulations, using the following spin Hamiltonian parameters: $|D| = 3.78$ cm^{-1}, $|E| = 0.064$ cm^{-1} ($E/D = 0.02$), $g = [2.00, 2.01, 2.02]$. Blue trace: $D < 0$; red trace: $D > 0$. The resonance at 11.7 T marked with the asterisk could not be attributed to the $S = 2$ spin system under study and, therefore, is not simulated.

HFEPR spectra of **5** gave spin Hamiltonian parameters in agreement with those previously reported and was thus not extensively studied here. In the case of **6**, a complete set of multifrequency spectra was recorded. Analysis of this two-dimensional (2-D) field-frequency dependence,[36] shown in Figure 4, gave the full set of spin Hamiltonian parameters, which were similar, but not identical to those of **5**, showing the sensitivity of ZFS parameters to small structural/electronic changes. Full details are given in the Supporting Information. These results also serve as an experimental calibration for the electronic structure calculations discussed below.

A LFT analysis of the electronic absorption spectra of **5** agrees with Albela et al., but also provided both crystal-field (as

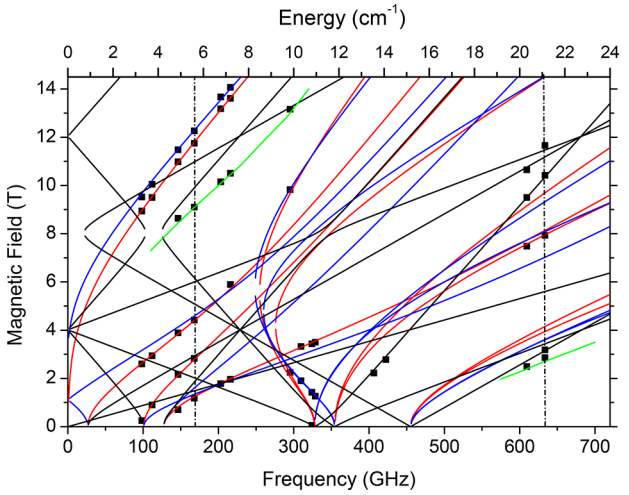

Figure 4. A 2-D map of turning points in the powder spectra of **6**, as a function of frequency. Solid squares (■) represent experimental points, and curves represent simulations. Red curves: magnetic field B_0 parallel to the x-axis of the ZFS tensor, blue curves: $B_0 \parallel y$; black curves $B_0 \parallel z$; green curves: off-axis turning points. The simulation parameters were $|D| = 3.79$ cm^{-1}, $|E| = 0.15$ cm^{-1} ($E/D = 0.04$), $g = [1.94, 2.08, 2.02]$. Fixing the g values to a more physically reasonable $g_{iso} = 2.00$ yielded only slightly lower-quality fits and did not change the D value, but resulted in a twice as small $|E| = 0.07$ cm^{-1} ($E/D = 0.02$, see Figure 3). The dashed vertical lines represent the frequencies at which spectra shown in Figures S14 (lower frequency) and 3 (higher frequency) were recorded.

defined by Ballhausen) and AOM parameters quantifying the bonding of the pyridinophane ligand. Full details are given in the Supporting Information. QCT investigation of several complex cations of the general formula $[(Py_2(NR)_2)MnX_2]^+$ (R = Me, Cy; X = F, Cl, OH) clearly show the spin quintet ground state with the "hole" in d_{xy}, in agreement with the earlier DFT calculations on **5** (see Figure 5).[17] The reported sa-CASSCF-

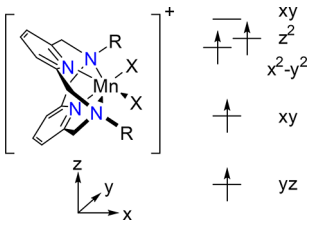

Figure 5. Qualitative d-orbital manifold for $[(Py_2(NR)_2)MnX_2]^+$ complexes.

(4,5)-based calculations lead to D values ranging from −3.8 cm^{-1} to −4.0 cm^{-1} when taking into account the spin−spin coupling (SSC) interaction (using MRCI) and NEVPT2 dynamic electron correlation effects, where the SSC contribution is ∼5 times larger (−0.5 cm^{-1}) than dynamic electron correlation effects (−0.1 cm^{-1}) in the case of the optimized geometries (see Tables S5 and S6 in the Supporting Information).[37] The BLYP DFT method underestimates the D parameter by ca. 1 cm^{-1}, and B3LYP results are even less satisfactory, see Tables S5 and S6. Full details of the QCT studies are given in the Supporting Information, which also provides frontier B3LYP MO diagrams of complexes of interest (see Figure S19 in the Supporting Information). Importantly, the calculations show that $[(Py_2NR_2)Mn(OH)_2]^+$, which is

DOI: 10.1021/acs.inorgchem.7b02421
Inorg. Chem. 2017, 56, 14315−14325

proposed as an intermediate in water oxidation,[28] has the same electronic structure as $[(Py_2NR_2)MnX_2]^+$ (X = F, Cl). Thus, the properties of the latter complexes are expected to provide a good model for those of $[(Py_2(NR)_2)Mn(OH)_2]^+$, which has so far eluded experimental detection. Furthermore, the DFT and CASSCF(4,5) electron configurations are qualitatively in agreement with each other, where the single DFT determinant (d-populations for charge and spin density, localized orbitals, or unrestricted natural orbitals) has the same structure as the one dominant determinant of the state specific CASSCF(4,5) wave function (d-populations for charge and spin density, active natural orbitals). This agreement can be seen, e.g., in the d-populations listed in Table S3 (Supporting Information). Hence, the DFT computations give a reliable picture of the electronic structure of the known complexes $[(Py_2NR_2)MnX_2]^+$ (X = F, Cl) as well as the hypothetical complex, potentially of catalytic interest, $[(Py_2(NR)_2)Mn(OH)_2]^+$.

Electrochemical Studies. The electrochemical properties of **1**−**4** were investigated in NBu_4PF_6/MeCN, with all potentials referenced to Fc^+/Fc (Table 3). As illustrated by the cyclic voltammogram of **4** (Figure 6), all complexes show one quasi-reversible reductive and one reversible oxidative process, with complexes **1** and **4** showing an additional quasi-reversible oxidative process at higher potential. This second oxidative process is irreversible for **2** and **3** (see Figures S8−S10 in the Supporting Information).

Since the Zn analogue, $[(Py_2N^tBu_2)Zn(OTf)(NCMe)]^+$, shows a reduction event at ca. −2 V vs Fc^+/Fc that has been assigned as a ligand-based reduction,[38] we have likewise assigned the quasi-reversible reductive processes to ligand-based reduction. The first oxidative wave is assigned to the Mn^{III}/Mn^{II} couple, which is confirmed through independent synthesis (see below) and the second quasi-reversible oxidation wave is tentatively assigned to the Mn^{IV}/Mn^{III} couple. The electrochemical data clearly shows the superior ability of $Py_2N^tBu_2$ to stabilize Mn(III) (Table 3). Notably, the Mn^{III}/Mn^{II} and Mn^{IV}/Mn^{III} potentials for all these complexes are at a significantly higher potential than that observed for analogous manganese complexes of dimethyl-substituted cross-bridged tetraazamacrocycle complexes ((BCA)$MnCl_2$ and (BCE)-$MnCl_2$, Figure S12 in the Supporting Information): $E_{1/2}$ (Mn^{III}/Mn^{II}) is −0.055 V for (BCA)$MnCl_2$ and −0.174 V for (BCE)$MnCl_2$; $E_{1/2}$ (Mn^{IV}/Mn^{III}) is +0.703 V for (BCA)$MnCl_2$ and +0.592 V for (BCE)$MnCl_2$.[39] The difference in potentials is likely due to the different donor strengths of these macrocycles, all of which create a *cis*-divacant coordination environment.

The reversibility of the first oxidative process observed in the CV of **4** has been confirmed by chemical oxidation. Treating **4** with the thianthrenyl cation (Th·BF_4, $E_{1/2}$ = 0.86 V vs Fc^+/Fc)[40] results in an immediate color change from pale yellow to dark orange (Scheme 3). The oxidized product is characterized as $[(Py_2N^tBu)MnCl_2]BF_4$ (**9**) by ESI-MS and single-crystal XRD, with the structure shown in Figure 7. The UV-vis spectrum of **9** shows a band at ∼500 nm, similary to the spectroscopically characterized complex $[(Py_2NMe_2)MnCl_2]^+$ (Figure S7 in the Supporting Information).[17] The magnetic

Table 3. Redox Potentials ($E_{1/2}$) for 1−4 (vs Fc/Fc^+)

	Py/Py•	Mn^{III}/Mn^{II}	Mn^{IV}/Mn^{III}
1	−2.37	0.16	1.24
2	−2.37	0.20	1.38[a]
3	−2.32	0.21	1.29[a]
4	−2.28	0.04	1.40

[a]Irreversible waves; E_{pa} values are shown.

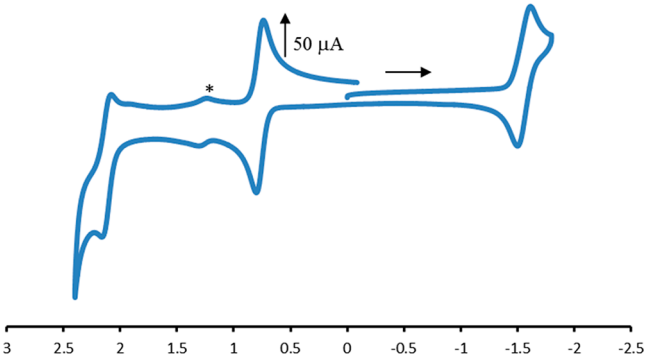

Figure 6. Cyclic voltammogram of **4** recorded at room temperature in MeCN solution. GC electrode, 0.1 M NBu_4PF_6 as an electrolyte (scan rate = 100 mV/s). Asterisk (*) denotes a peak that can be attributed to an impurity.

Scheme 3. Formation of $[(Py_2N^tBu_2)Mn^{III}Cl_2]^+$ (9) via the Chemical Oxidation of 4

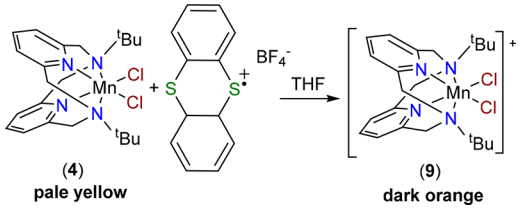

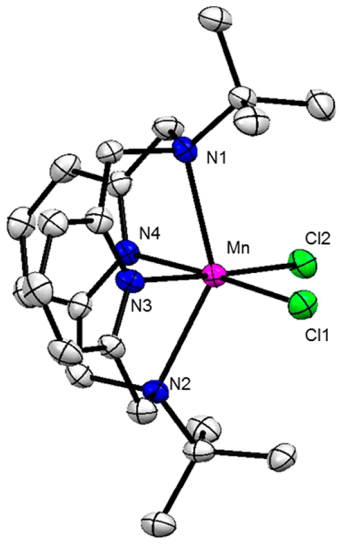

Figure 7. ORTEP diagram of **9** (50% ellipsoids; hydrogen atoms and PF_6 anions are omitted for the sake of clarity). Selected bond lengths: Mn−N1, 2.392(3) Å; Mn−N2, 2.396(3) Å; Mn−N3, 2.028(3) Å; Mn−N4, 2.014(4) Å; Mn−Cl1, 2.242(1) Å; and Mn−Cl2, 2.236(1) Å. Selected bond angles (deg): N1−Mn−N2, 142.8(1)°; N3−Mn−N4, 85.4(1)°; and Cl1−Mn−Cl2, 93.94(4)°.

DOI: 10.1021/acs.inorgchem.7b02421
Inorg. Chem. 2017, 56, 14315−14325

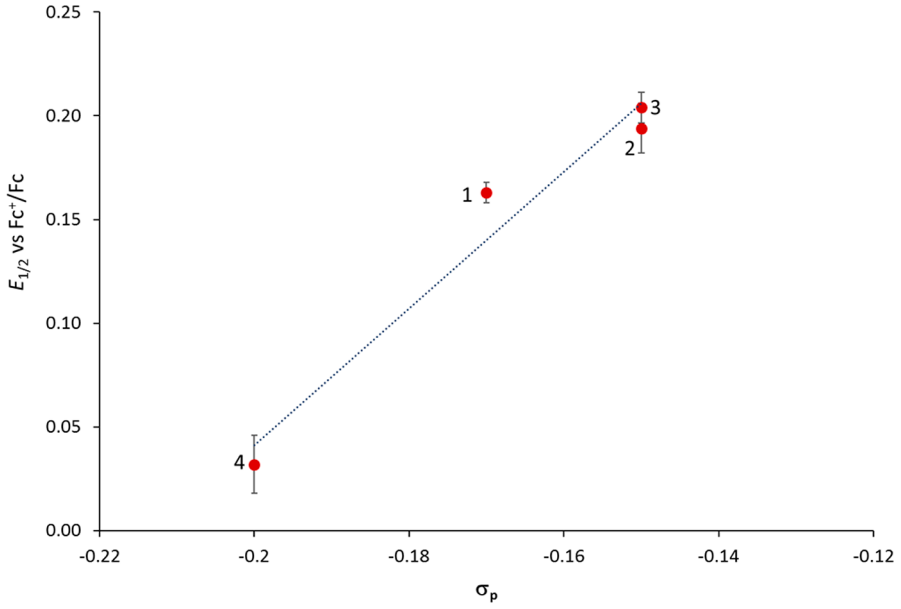

Figure 8. $E_{1/2}(Mn^{III}/Mn^{II})$ for **1**−**4** vs Hammett values (σ_p) of the amine substituents. Plot fits to the equation $y = 3.2687x + 0.7$ ($R^2 = 0.9793$) are shown.

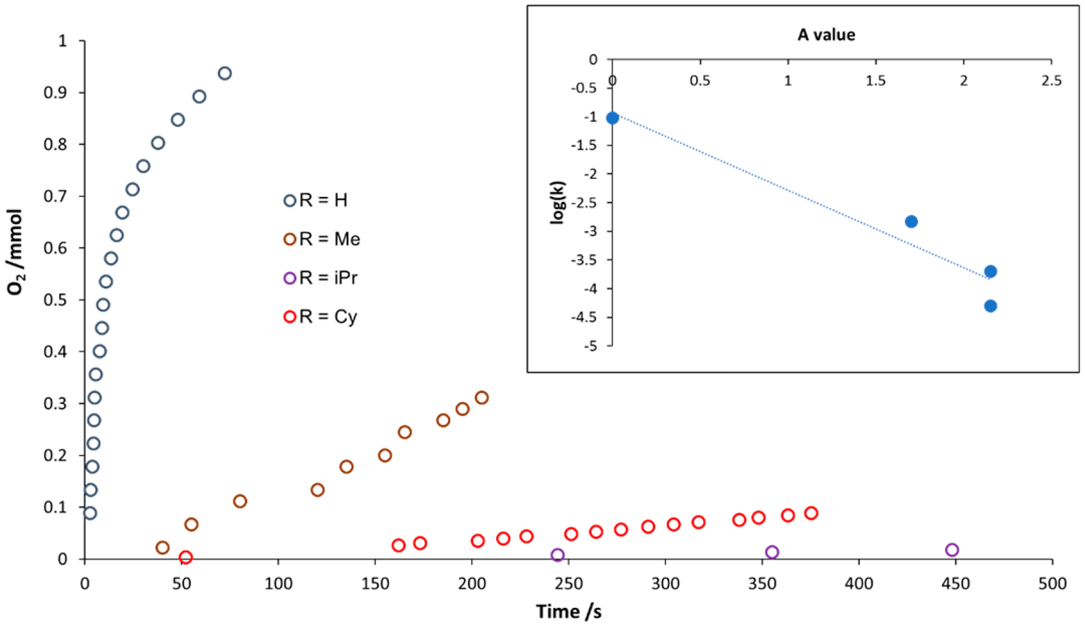

Figure 9. Oxygen formation by H_2O_2 disproportionation catalyzed by $Py_2NH_2MnCl_2$ and complexes **1**−**3**. Initial conditions: $[(Py_2NR_2)MnCl_2]$ = 0.4 mM, $[H_2O_2]$ = 3.1 M, pH 7.0, 298 K. Inset: plot of log(k) vs A value (k: initial rate of O_2 formation). Plot fits to the equation $y = -1.3497x - 0.937$ ($R^2 = 0.9335$). Note that the error bars are too small to be observed in this plot.

susceptibility of **9**, as measured via the Evans method (μ_{eff} = 5.05 μB), is consistent with high spin (S = 2) Mn(III).

In order to delineate the effect of the pyridinophane ligand substituents on the stability of higher oxidation states, we analyzed the Mn^{III}/Mn^{II} electrochemical data, in terms of steric and electronic parameters. While $E_{1/2}$ does not correlate well with the steric parameter of the ligand substituent, as measured by the A value (Figure S13 in the Supporting Information),[41,42] there is a good linear relationship with the Hammett parameter (σ_p; see Figure 8).[43,44] This suggests that the donor strength of the pyridinophane ligand is the key factor that affects the stability of the Mn(III) oxidation state, despite the significant effect of substituent sterics on the molecular structures (Tables 1 and 2). A caveat to this conclusion is that these substituents represent a very small range of σ_p values and thus may not hold over a wider range of donor strengths.

Catalytic Activity in O_2 Evolution. We have previously demonstrated that complex **1** is catalytically active toward H_2O_2 disproportionation, whereas $(Py_2N^tBu_2)MnCl_2$ is not.[10] On the other hand, complex **4** is active in electrocatalytic oxidation of H_2O to O_2, whereas **1** is not.[9] To better delineate the effect of pyridinophane ligand substitution on these catalytic reactions, we investigated the reactivity of **2** and **3** toward both H_2O_2 disproportionation and H_2O oxidation.

The catalytic reactivity toward H_2O_2 disproportionation of complexes **1**−**3**, along with $(Py_2NH_2)MnCl_2$,[9] shows that the

DOI: 10.1021/acs.inorgchem.7b02421
Inorg. Chem. 2017, 56, 14315−14325

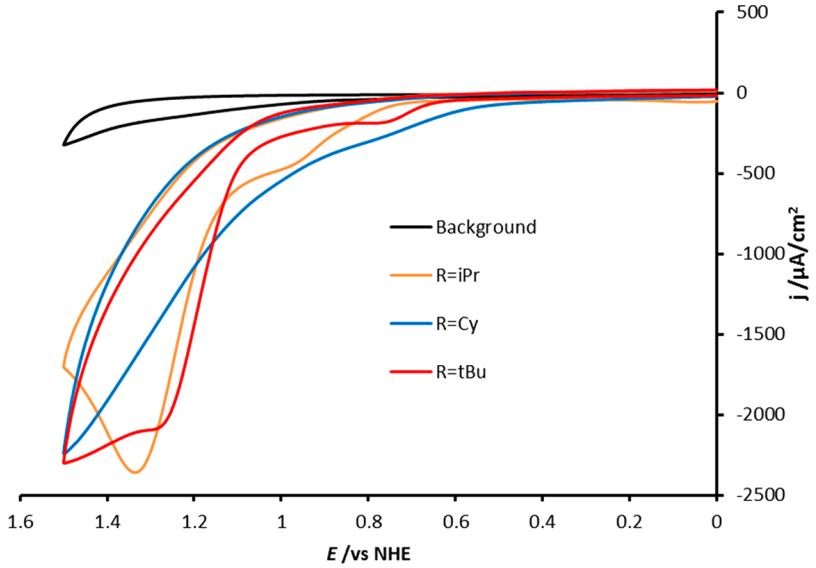

Figure 10. Cyclic voltammograms of solution without $(Py_2NR_2)MnCl_2$ complex (black), and with Mn(II) complexes at 0.5 mM: R = $^{i}Pr_2$ (**2**) (orange), R = Cy (**3**) (blue), R = ^{t}Bu (**4**) (red), all at pH 12.2; GC electrode; 50 mM KOTf; scan rate = 100 mV/s.

rate of O_2 formation has a clear dependence on the pyridinophane substituent (Figure 9): bulkier substituents significantly slow the rate of reaction, with **4**, which has the bulkiest substituents, being inactive. The linear relationship between log(k) and the steric parameter (A value)[41] confirms that ligand bulkiness is critical to the rate of catalysis (Figure 8, inset).

We have used cyclic voltammetry (CV) to investigate the ability of complexes **1**[9]**–4** toward electrocatalytic H_2O oxidation (Figure 10). At pH 12.2, the cyclic voltammograms of **2** and **3** exhibit either a large oxidation wave (complex **2**) or enhanced current (complex **3**), suggesting that both are active toward H_2O oxidation at similar overpotential to **4**.[45]

Previous computational investigations into the mechanism of catalytic H_2O oxidation by **4** implicate the formation of high valent Mn-oxo/oxyl species as precursors to O–O coupling and consequent O_2 generation.[28,29] Since the overpotential for water oxidation depends on the accessibility of these species, the pyridinophane substituents may be expected to play an important role in the energetics of catalysis by stabilizing these intermediates. Using the Mn^{III}/Mn^{II} couple as an indicator for the accessibility of higher oxidation states, it is notable that there is no relationship between the onset of catalytic activity and $E_{1/2}(Mn^{III}/Mn^{II})$, and, consequently, the donor strength of the ligand (c.f. Figure 8). For example, despite complex **4** having the lowest $E_{1/2}(Mn^{III}/Mn^{II})$ (by over 0.1 V), the onset of catalysis is similar to that observed for complexes **2** and **3**. Moreover, although $E_{1/2}(Mn^{III}/Mn^{II})$ for **1** is at a lower potential than for **2** or **3**, this complex shows no evidence for H_2O oxidation catalysis.[9] Thus, the activity of these complexes for electrocatalytic water oxidation cannot be related to simple electronic effects.

Despite the apparent lack of ligand electronic effect on water oxidation catalysis, it is evident that only the complexes with smaller pyridinophane ligand substituents, i.e., $(Py_2NH_2)MnCl_2$ and **1**, are not catalytically active. However, there is no simple relationship between the pyridinophane substituent size and any electrochemical parameter (e.g., onset potential or peak current). Thus, although there appears to be a steric threshold for achieving water oxidation electrocatalysis, the catalytic activity of $(Py_2NR_2)MnCl_2$ complexes cannot be related to simple steric or electronic factors.

SUMMARY AND CONCLUSIONS

A series of Mn(II) and Mn(III) complexes bearing pyridinophane ligands with different substituents have been prepared and characterized. While a relationship between the size of the pyridinophane amine substituent and the metrical parameters of the Mn(II) complexes (**1**–**4**) was observed, no such trend was observed for the structures of the Jahn–Teller distorted Mn(III) complexes (**5**–**8**). HFEPR spectroscopy of **6** is characteristic for six-coordinate high-spin Mn(III), in terms of having a negative D value of modest magnitude: D = −3.79 cm^{-1}, with slight rhombicity $|E/D|$ = .0.02–0.04. Computational investigation at an ab initio level of theory are fully consistent with experiment, providing calculated D values in the range from −3.8 cm^{-1} to −4.0 cm^{-1}. The cyclic voltammograms of the Mn(II) complexes reveal reversible Mn^{III}/Mn^{II} redox couples, which has been synthetically confirmed through the synthesis and characterization of $[(Py_2N^{t}Bu_2)MnCl_2]BF_4$ (**9**). The stability of the Mn(III) state was found to be directly related to the donor strength of pyridinophane ligand substituents.

The donor strength of the ligand is critical for accessing higher Mn oxidation states, therefore suggesting that the pyridinophane ligand platform, in general terms, is well-suited for H_2O/H_2O_2 activation catalysis. What is also apparent, however, is that rather than further tuning the donor properties of this platform, the size of the ligand is also critical, as seen in comparing the catalytic activity of **1**–**4**. In the case of H_2O_2 disproportionation, the rate of reaction decreases as the size of the R group increases, while electrocatalytic water oxidation was observed for complexes only having bulky ligand substituents. The relative insensitivity to electronic effects, albeit for a small range of donor strengths, bodes well for similarly converting other H_2O_2 disproportionation catalysts to water oxidation catalysts through increase in ligand bulk, similar to the tuning achieved of the organic substituents in widely used ligands such as phosphines, pyrazolyl(borates), and *N*-heterocyclic carbenes.

DOI: 10.1021/acs.inorgchem.7b02421
Inorg. Chem. 2017, 56, 14315–14325

EXPERIMENTAL SECTION

General Considerations. All anaerobic manipulations, including nonaqueous electrochemical measurements, were performed under a nitrogen atmosphere by using standard Schlenk techniques or in an M. Braun Labmaster glovebox. Glassware was dried at 150 °C overnight. Organic solvents were purified by the Glass Contour solvent system. Deionized water was used for all aqueous experiments or measurements. ^{1}H NMR data were recorded on a Varian Unity 400 spectrometer (400 MHz) at 22 °C. UV-vis spectra were recorded with an Agilent Cary 60 UV-vis spectrometer. High resolution mass spectra were recorded using positive electrospray ionization on a Thermo Electron Corp MAT-95XP spectrometer. Trifluoroacetic acid (CF_3COOH) was used as protonation agent for neutral complexes. Solution magnetic susceptibilities were determined using the Evans method.[46] Electrochemical measurements were recorded on an electrochemical analyzer (Model CHI 600D, CH Instruments). A glassy carbon (GC) electrode (3 mm × 3 mm, CH Instruments) was used as the working electrode, a platinum wire (Alfa Aesar, 99.99%) was used as the auxiliary electrode, and a silver wire (Alfa Aesar, 99.99%) was used as the pseudoreference electrode. The final redox potentials were calculated by comparing the measured potentials with $E_{1/2}$ of Fc/Fc^+ in the same solution. The reproducibility of all cyclic voltammetry experiments are verified by several repeat scans.

Synthesis of Compounds. The compounds of 2,6-bis-(bromomethyl)pyridine,[47] *N,N′*-dimethyl-2,11-diaza[3,3](2,6)-pyridinophane (Py_2NMe_2), 2,11-diaza[3,3](2,6)-pyridinophane (Py_2NH_2),[48] **1** and **5**,[17] *N,N′*-di-isopropyl-2,11-diaza[3,3](2,6)-pyridinophane ($Py_2N^iPr_2$),[38] **1′**,[10] **4′**,[9] and thianthrenyl cation ($Th^{\bullet+}BF_4^-$)[49] were prepared according to literature procedures. All other compounds were obtained from commercial suppliers and used as received.

Preparation of $Py_2N^tBu_2$ Ligand. The synthesis of *N,N′*-di-*tert*-butyl-2, 11-diaza[3,3](2,6)-pyridinophane ($Py_2N^tBu_2$) was adapted from reported literature procedures.[50] *tert*-Butylamine (7.61 mL, 71 mmol, 9 equiv) was added to a solution of 2,6-dibromomethylpyridine (2.1 g, 7.92 mmol) in benzene (200 mL) and water (500 mL) at ambient temperature. The resulting solution of mixture was heated at 80 °C overnight, then cooled to room temperature. After spontaneous separation, the organic phase was washed with water (2 × 100 mL) and dried over sodium sulfate. The solvent was then removed by vacuum evaporation to yield a sticky solid. After washing with hexane, the solid was subjected to chromatography (column, SiO_2) by eluting with dichloromethane containing increasing concentrations of triethylamine (0−5%) to yield $Py_2N^tBu_2$ as a white solid (150 mg, 11% based on 2,6-dibromomethylpyridine). The spectral properties are identical to those reported in the literature.[50] ^{1}H NMR ($CDCl_3$, 400 MHz): δ 1.37 (18H, s, CH_3); 3.97 (8H, s, $PyCH_2$); 6.68−6.76 (4H, d, 3,5-Py H); and 6.91−7.27 (2H, m, 4-Py H).

Preparation of Py_2NCy_2 Ligand. Py_2NCy_2 is prepared according to a modified procedure from the literature.[16] A 125 mL RB flask was charged with Py_2NH_2 (0.048 g, 0.50 mmol), cyclohexyl bromide (3 mL, 50 mmol, 100 equiv), anhydrous K_2CO_3 (1.38 g, 10 mmol, 20 equiv) and dry MeCN (50 mL). The reaction was heated at reflux under a nitrogen atmosphere for 7 days. The solution was then cooled to RT and the solvent was removed under reduced pressure. The residue was suspended in CH_2Cl_2 (50 mL) and then washed with 1 M NaOH (2 × 50 mL) solution and water (2 × 50 mL). The CH_2Cl_2 layer was isolated, dried over anhydrous $MgSO_4$, evaporated, and further dried under vacuum to give an off-white powder (0.56 g, 69% based on Py_2NH_2). The spectra properties are identical to those reported in the literature.[16]

Preparation of $(Py_2NR_2)MnCl_2$ Complexes. Complexes **2**, **3**, and **4** were prepared by adding $MnCl_2$ to a stirred solution of Py_2NR_2 ligand in MeCN. After stirring overnight at room temperature, (Py_2NR_2)-$MnCl_2$ was obtained as pale yellow solid after removing the solvent under vacuum. Crystals suitable for single-crystal XRD were directly obtained by slow diffusion of diethyl ether into MeCN solutions of the complexes. Yields for **2** (70%), **3** (66%), **4** (58%) were based on Py_2NR_2 ligand. The complexes were characterized in MeCN solution by HRMS (ESI): calcd for $(Py_2NR_2)MnCl_2$ complexes: **2**: ($C_{20}H_{28}ClMnN_4$) *m/z*: 414.1383 ($[M\text{-}Cl]^+$); found: 414.1366; **3**: ($C_{26}H_{36}MnN_4CF_3COO$) *m/z*: 572.2171 ($[M\text{-}CF_3COO]^+$); found: 572.2167; **4**: $C_{22}H_{32}MnN_4CF_3COO$ *m/z*: 520.1858 ($[M\text{-}CF_3COO]^+$); found: 520.1860.

*Preparation of **2′**.* Complex **2′** was synthesized by treating **2** (23 mg, 0.05 mmol) with $TlPF_6$ (35 mg, 0.1 mmol) in acetonitrile (10 mL). After stirring at room temperature overnight, the reaction mixture was filtered and the solvent was removed under reduced pressure to yield an off-white powder (44 mg, 60% based on **2**). *[Caution: $TlPF_6$ is extremely toxic and appropriate personal protective equipment is required.]*

*Preparation of **6**, **7**, and **8**.* Under anaerobic conditions, **2′**, **3′**, and **4′** (0.045 mmol, 1 equiv) were mixed with XeF_2 (0.048 mmol, 1.05 equiv) in acetonitrile (10 mL). The mixtures were stirred overnight to yield red−brown solutions, which were concentrated under reduced pressure to ca. 5 mL. Red−orange crystals of **6** and **8** suitable for single-crystal XRD were obtained by slow diffusion of diethyl ether into these solutions. Yields for **6** (40%), **7** (30%), **8** (45%) were based on **2′**, **3′**, and **4′**, respectively. Complexes were characterized in MeCN solution by HRMS (ESI): calcd for $[(Py_2NR_2)MnF_2]^+$ complexes: **6**: ($C_{20}H_{28}MnN_4F_2$) *m/z*: 417.1663 ($[M]^+$); found: 417.1665; **7**: ($C_{26}H_{36}MnN_4F_2$) *m/z*: 497.2289 ($[M]^+$); found: 497.2282; **8**: $C_{22}H_{32}MnN_4F_2$ *m/z*: 445.1975 ($[M]^+$); found: 445.1979. UV-vis (CH_3CN): λ_{max} (ε/L mol^{-1} cm^{-1}) = 468 (92), 489 (89) nm for **2**; 468 (133), 494 (130) nm for **3**; 465 (134), 501 (189) nm for **4**.

*Synthesis of **6** from MnF_3.* The $Py_2N^iPr_2$ ligand (20 mg, 0.05 mmol) was added to a slurry of MnF_3 (5.6 mg, 0.05 mmol) in MeOH (15 mL). The mixture was then warmed at 50 °C until the yellow-cloudy solution became clear brown (ca. 4 h). Aqueous $NaPF_6$ (5 mL, 16.8 mg, 0.1 mmol) was then added to the solution, which was dried under reduced pressure to give a brown residue. The product was extracted into 10 mL dichloromethane and the solvent was removed under reduced pressure to give **6** as a brown powder (10 mg, 30% based on the amount of $Py_2N^iPr_2$ ligand). An orange crystal for single-crystal XRD was obtained through slow diffusion of pentane into a concentrated dichloromethane solution at ambient temperature. The spectra properties are identical to the characterizations of **6** prepared through XeF_2 fluorination described above.

*Preparation of **9**.* Under anaerobic conditions, $Th^{\bullet+}BF_4^-$ (19 mg, 0.06 mmol) was added to a solution of $(Py_2N^tBu_2)MnCl_2$ (25 mg, 0.05 mmol) in THF (15 mL). The reaction was further stirred at room temperature overnight until the yellow slurry change to red, filtered through Celite, and washed with THF (5 mL) to afford a dark orange solid. Dark orange crystals of **9** suitable for single crystal X-ray diffraction were obtained by slow diffusion of diethyl ether into its acetonitrile solution. Yield: 11 mg, 40% based on $(Py_2N^tBu_2)MnCl_2$. Complex **9** was characterized in MeCN solution by HRMS (ESI): calcd for $C_{22}H_{32}Cl_2MnN_4$ *m/z*: 477.1385 ($[M]^+$); found: 477.1381. UV-vis (CH_3CN): λ_{max} (ε/L mol^{-1} cm^{-1}) = 494 (255), 518 (335) nm.

HFEPR Spectroscopy. HFEPR measurements were made using a spectrometer that has been described elsewhere.[51] The samples were investigated both as loose microcrystalline powders and compressed into pellets. HFEPR spectra were simulated with the program SPIN, from A. Ozarowski,[52] using a standard spin Hamiltonian for $S = 2$,[53] with only second-order ZFS terms.

Ligand-Field Theory. The programs Ligfield, from J. Bendix,[54] and DDN and DDNFIT,[55] from J. Telser, were used for LFT analysis of the Mn(III) complexes, as described in the Supporting Information.

Quantum Chemical Theory. Gaussian 09[56] software was used for B3LYP[57−60]/6-311+G*[61−63] geometry optimizations of Mn(III) complexes, as well as for the production of particular molecular orbitals (MOs) (as shown in the Supporting Information). The ORCA program package devised by F. Neese and co-workers (version 3.0.0)[64,65] was used for calculation of spin Hamiltonian parameters, specifically employing CASSCF,[18,20−23] NEVPT2,[24−26] and MRCI[18,20,27] methods. Further details are given in the Supporting Information.

DOI: 10.1021/acs.inorgchem.7b02421
Inorg. Chem. 2017, 56, 14315−14325

■ ASSOCIATED CONTENT

Supporting Information

The Supporting Information is available free of charge on the ACS Publications website at DOI: 10.1021/acs.inorgchem.7b02421.

Experimental figures, discussion of ligand-field theory analysis of $[(Py_2NMe_2)MnF_2]^+$ and quantum chemical theory; and crystallographic data collection (PDF)

Accession Codes

CCDC 1576812−1576817 contain the supplementary crystallographic data for this paper. These data can be obtained free of charge via www.ccdc.cam.ac.uk/data_request/cif, or by emailing data_request@ccdc.cam.ac.uk, or by contacting The Cambridge Crystallographic Data Centre, 12 Union Road, Cambridge CB2 1EZ, U.K.; fax: +44 1223 336033.

■ AUTHOR INFORMATION

Corresponding Author

*Tel.: 812-856-4119. Fax: 812-855-8300. E-mail: smith962@indiana.edu.

ORCID

Lukas Bucinsky: 0000-0002-0190-3231
Joshua Telser: 0000-0003-3307-2556
Jeremy M. Smith: 0000-0002-3206-4725

Notes

The authors declare no competing financial interest.

■ ACKNOWLEDGMENTS

S.X. and J.M.S. acknowledge funding from Indiana University and the National Science Foundation (NSF) (No. CHE-1566258). A portion of this work was performed at the National High Magnetic Field Laboratory, which is supported by NSF Cooperative Agreement No. DMR-1157490 and the State of Florida. We thank Dr. Andrew Ozarowski for his EPR fit and simulation software SPIN. M.B and L.B. acknowledge support from the Slovak Science and Technology Assistance Agency, under Contract Nos. APVV-15-0053 and APVV-15-0079, and the Slovak Grant Agency VEGA, under Contract Nos. 1/0598/16 and 1/0416/17. We thank the HPC Center at the Slovak University of Technology in Bratislava, which is a part of the Slovak Infrastructure of High Performance Computing (SIVVP Project, ITMS Code 26230120002, funded by the European Region Development Funds), for computing facilities.

■ DEDICATION

Dedicated to Professor Dr. Karl Wieghardt on the occasion of his 75th birthday anniversary.

■ REFERENCES

(1) Blakemore, J. D.; Crabtree, R. H.; Brudvig, G. W. Molecular Catalysts for Water Oxidation. *Chem. Rev.* **2015**, *115* (23), 12974−13005.

(2) Meyer, T. J. Chemical approaches to artificial photosynthesis. *Acc. Chem. Res.* **1989**, *22* (5), 163−170.

(3) Gray, H. B. Powering the planet with solar fuel. *Nat. Chem.* **2009**, *1* (1), 7−7.

(4) Umena, Y.; Kawakami, K.; Shen, J.-R.; Kamiya, N. Crystal structure of oxygen-evolving photosystem II at a resolution of 1.9 Å. *Nature* **2011**, *473* (7345), 55−60.

(5) Yano, J.; Yachandra, V. Mn_4Ca Cluster in Photosynthesis: Where and How Water is Oxidized to Dioxygen. *Chem. Rev.* **2014**, *114* (8), 4175−4205.

(6) Suga, M.; Akita, F.; Hirata, K.; Ueno, G.; Murakami, H.; Nakajima, Y.; Shimizu, T.; Yamashita, K.; Yamamoto, M.; Ago, H.; Shen, J.-R. Native structure of photosystem II at 1.95 Å resolution viewed by femtosecond X-ray pulses. *Nature* **2014**, *517* (7532), 99−103.

(7) Kanady, J. S.; Lin, P.-H.; Carsch, K. M.; Nielsen, R. J.; Takase, M. K.; Goddard, W. A.; Agapie, T. Toward Models for the Full Oxygen-Evolving Complex of Photosystem II by Ligand Coordination To Lower the Symmetry of the Mn_3CaO_4 Cubane: Demonstration That Electronic Effects Facilitate Binding of a Fifth Metal. *J. Am. Chem. Soc.* **2014**, *136* (41), 14373−14376.

(8) Najafpour, M. M.; Renger, G.; Hołyńska, M.; Moghaddam, A. N.; Aro, E.-M.; Carpentier, R.; Nishihara, H.; Eaton-Rye, J. J.; Shen, J.-R.; Allakhverdiev, S. I. Manganese Compounds as Water-Oxidizing Catalysts: From the Natural Water-Oxidizing Complex to Nanosized Manganese Oxide Structures. *Chem. Rev.* **2016**, *116* (5), 2886−2936.

(9) Lee, W.-T.; Muñoz, S. B.; Dickie, D. A.; Smith, J. M. Ligand Modification Transforms a Catalase Mimic into a Water Oxidation Catalyst. *Angew. Chem., Int. Ed.* **2014**, *53* (37), 9856−9859.

(10) Lee, W.-T.; Xu, S.; Dickie, D. A.; Smith, J. M. A Robust Mn Catalyst for H_2O_2 Disproportionation in Aqueous Solution. *Eur. J. Inorg. Chem.* **2013**, *2013* (22−23), 3867−3873.

(11) Signorella, S.; Hureau, C. Bioinspired functional mimics of the manganese catalases. *Coord. Chem. Rev.* **2012**, *256* (11), 1229−1245.

(12) Chow, T. W.-S.; Wong, E. L.-M.; Guo, Z.; Liu, Y.; Huang, J.-S.; Che, C.-M. *cis*-Dihydroxylation of Alkenes with Oxone Catalyzed by Iron Complexes of a Macrocyclic Tetraaza Ligand and Reaction Mechanism by ESI-MS Spectrometry and DFT Calculations. *J. Am. Chem. Soc.* **2010**, *132* (38), 13229−13239.

(13) Koch, W. O.; Krüger, H.-J. A Highly Reactive and Catalytically Active Model System for Intradiol-Cleaving Catechol Dioxygenases: Structure and Reactivity of Iron(III) Catecholate Complexes of *N*,*N*′-Dimethyl-2,11-diaza[3.3](2,6)pyridinophane. *Angew. Chem., Int. Ed. Engl.* **1996**, *34* (23−24), 2671−2674.

(14) Zheng, B.; Tang, F.; Luo, J.; Schultz, J. W.; Rath, N. P.; Mirica, L. M. Organometallic Nickel(III) Complexes Relevant to Cross-Coupling and Carbon−Heteroatom Bond Formation Reactions. *J. Am. Chem. Soc.* **2014**, *136* (17), 6499−6504.

(15) Krüger, H.-J. Spin transition in octahedral metal complexes containing tetraazamacrocyclic ligands. *Coord. Chem. Rev.* **2009**, *253* (19), 2450−2459.

(16) Kim, J.; Shin, B.; Kim, H.; Lee, J.; Kang, J.; Yanagisawa, S.; Ogura, T.; Masuda, H.; Ozawa, T.; Cho, J. Steric Effect on the Nucleophilic Reactivity of Nickel(III) Peroxo Complexes. *Inorg. Chem.* **2015**, *54* (13), 6176−6183.

(17) Albela, B.; Carina, R.; Policar, C.; Poussereau, S.; Cano, J.; Guilhem, J.; Tchertanov, L.; Blondin, G.; Delroisse, M.; Girerd, J.-J. Synthesis and X-ray Structure of the $Mn^{II}Cl_2$ and $Mn^{III}F_2$ Complexes of *N*,*N*′-Dimethyl-2,11-diaza[3,3](2,6)pyridinophane. High-Field Electron Paramagnetic Resonance and Density Funtional Theory Studies of the Mn(III) Complex. Evidence for a Low-Lying Spin Triplet State. *Inorg. Chem.* **2005**, *44* (20), 6959−6966.

(18) Neese, F. Importance of Direct Spin−Spin Coupling and Spin-Flip Excitations for the Zero-Field Splittings of Transition Metal Complexes: A Case Study. *J. Am. Chem. Soc.* **2006**, *128* (31), 10213−10222.

(19) Neese, F. Calculation of the zero-field splitting tensor on the basis of hybrid density functional and Hartree-Fock theory. *J. Chem. Phys.* **2007**, *127* (16), 164112.

(20) Duboc, C.; Ganyushin, D.; Sivalingam, K.; Collomb, M.-N.; Neese, F. Systematic Theoretical Study of the Zero-Field Splitting in Coordination Complexes of Mn(III). Density Functional Theory versus Multireference Wave Function Approaches. *J. Phys. Chem. A* **2010**, *114* (39), 10750−10758.

(21) Zein, S.; Neese, F. Ab Initio and Coupled-Perturbed Density Functional Theory Estimation of Zero-Field Splittings in Mn^{II}

DOI: 10.1021/acs.inorgchem.7b02421
Inorg. Chem. 2017, 56, 14315−14325

Transition Metal Complexes. *J. Phys. Chem. A* **2008**, *112* (34), 7976−7983.
(22) Romain, S.; Duboc, C.; Neese, F.; Rivière, E.; Hanton, L. R.; Blackman, A. G.; Philouze, C.; Leprêtre, J.-C.; Deronzier, A.; Collomb, M.-N. An Unusual Stable Mononuclear Mn^{III} Bis-terpyridine Complex Exhibiting Jahn−Teller Compression: Electrochemical Synthesis, Physical Characterisation and Theoretical Study. *Chem. - Eur. J.* **2009**, *15* (4), 980−988.
(23) Maurice, R.; Bastardis, R.; Graaf, C. d.; Suaud, N.; Mallah, T.; Guihéry, N. Universal Theoretical Approach to Extract Anisotropic Spin Hamiltonians. *J. Chem. Theory Comput.* **2009**, *5* (11), 2977−2984.
(24) Angeli, C.; Cimiraglia, R.; Evangelisti, S.; Leininger, T.; Malrieu, J.-P. Introduction of n-electron valence states for multireference perturbation theory. *J. Chem. Phys.* **2001**, *114* (23), 10252−10264.
(25) Angeli, C.; Cimiraglia, R.; Malrieu, J.-P. N-electron valence state perturbation theory: a fast implementation of the strongly contracted variant. *Chem. Phys. Lett.* **2001**, *350* (3), 297−305.
(26) Angeli, C.; Cimiraglia, R.; Malrieu, J.-P. *n*-electron valence state perturbation theory: A spinless formulation and an efficient implementation of the strongly contracted and of the partially contracted variants. *J. Chem. Phys.* **2002**, *117* (20), 9138−9153.
(27) Atanasov, M.; Zadrozny, J. M.; Long, J. R.; Neese, F. A theoretical analysis of chemical bonding, vibronic coupling, and magnetic anisotropy in linear iron(II) complexes with single-molecule magnet behavior. *Chem. Sci.* **2013**, *4* (1), 139−156.
(28) Crandell, D. W.; Xu, S.; Smith, J. M.; Baik, M.-H. Intramolecular Oxyl Radical Coupling Promotes O−O Bond Formation in a Homogeneous Mononuclear Mn-based Water Oxidation Catalyst: A Computational Mechanistic Investigation. *Inorg. Chem.* **2017**, *56* (8), 4435−4445.
(29) Li, Y.-Y.; Ye, K.; Siegbahn, P. E. M.; Liao, R.-Z. Mechanism of Water Oxidation Catalyzed by a Mononuclear Manganese Complex. *ChemSusChem* **2017**, *10* (5), 903−911.
(30) Dubinsky-Davidchik, I. S.; Potash, S.; Goldberg, I.; Vigalok, A.; Vedernikov, A. N. Electrophilic Fluorination of Organoplatinum(II) Iodides: Iodine and Platinum Atoms as Competing Fluorination Sites. *J. Am. Chem. Soc.* **2012**, *134* (34), 14027−14032.
(31) Brewer, S. A.; Coleman, K. S.; Fawcett, J.; Holloway, J. H.; Hope, E. G.; Russell, D. R.; Watson, P. G. Ruthenium and osmium acyl fluoride complexes. Crystal structure of $[OC\text{-}6\text{-}13]\text{-}[RuF_2(CO)_2(PPh_3)_2]\cdot CD_2Cl_2$. *J. Chem. Soc., Dalton Trans.* **1995**, *7*, 1073−1076.
(32) Barra, A.-L.; Gatteschi, D.; Sessoli, R.; Abbati, G. L.; Cornia, A.; Fabretti, A. C.; Uytterhoeven, M. G. Electronic structure of manganese(III) compounds from high-frequency EPR spectra. *Angew. Chem., Int. Ed. Engl.* **1997**, *36* (21), 2329−2331.
(33) Goldberg, D. P.; Telser, J.; Krzystek, J.; Montalban, A. G.; Brunel, L.-C.; Barrett, A. G. M.; Hoffman, B. M. EPR spectra from "EPR-silent" species: high-field EPR spectroscopy of manganese(III) porphyrins. *J. Am. Chem. Soc.* **1997**, *119*, 8722−8723.
(34) Krivokapic, I.; Noble, C.; Klitgaard, S.; Tregenna-Piggott, P. L. W.; Weihe, H.; Barra, A.-L. Anisotropic hyperfine interaction in the manganese(III) hexaaqua ion. *Angew. Chem., Int. Ed.* **2005**, *44* (23), 3613−3616.
(35) Vallejo, J.; Pascual-Álvarez, A.; Cano, J.; Castro, I.; Julve, M.; Lloret, F.; Krzystek, J.; De Munno, G.; Armentano, D.; Wernsdorfer, W.; Ruiz-García, R.; Pardo, E. Field-Induced Hysteresis and Quantum Tunneling of the Magnetization in a Mononuclear Manganese(III) Complex. *Angew. Chem., Int. Ed.* **2013**, *52* (52), 14075−14079.
(36) Krzystek, J.; Zvyagin, S. A.; Ozarowski, A.; Trofimenko, S.; Telser, J. Tunable-frequency high-field electron paramagnetic resonance. *J. Magn. Reson.* **2006**, *178* (2), 174−183.
(37) The SSC contribution is about two times larger (-0.5 cm^{-1}) than dynamic electron correlation effects in the case of the experimental geometry of **5**, see Table S5 (Supporting Information).
(38) Tang, F.; Qu, F.; Khusnutdinova, J. R.; Rath, N. P.; Mirica, L. M. Structural and reactivity comparison of analogous organometallic Pd(III) and Pd(IV) complexes. *Dalton Trans.* **2012**, *41* (46), 14046−14050.
(39) Hubin, T. J.; McCormick, J. M.; Collinson, S. R.; Buchalova, M.; Perkins, C. M.; Alcock, N. W.; Kahol, P. K.; Raghunathan, A.; Busch, D. H. New Iron(II) and Manganese(II) Complexes of Two Ultra-Rigid, Cross-Bridged Tetraazamacrocycles for Catalysis and Biomimicry. *J. Am. Chem. Soc.* **2000**, *122* (11), 2512−2522.
(40) Connelly, N. G.; Geiger, W. E. Chemical Redox Agents for Organometallic Chemistry. *Chem. Rev.* **1996**, *96* (2), 877−910.
(41) Muller, P. Glossary of terms used in physical organic chemistry (IUPAC Recommendations 1994). *Pure Appl. Chem.* **1994**, *66*, 1077.
(42) Winstein, S.; Holness, N. J. Neighboring Carbon and Hydrogen. XIX. t-Butylcyclohexyl Derivatives. Quantitative Conformational Analysis. *J. Am. Chem. Soc.* **1955**, *77* (21), 5562−5578.
(43) Hansch, C.; Leo, A.; Taft, R. W. A survey of Hammett substituent constants and resonance and field parameters. *Chem. Rev.* **1991**, *91* (2), 165−195.
(44) Conradie, M. M.; Conradie, J. Electrochemical behaviour of Tris(*β*-diketonato)iron(III) complexes: A DFT and experimental study. *Electrochim. Acta* **2015**, *152*, 512−519.
(45) Since rapid decomposition of complexes **2** and **3** was observed during bulk electrolysis, further investigations into their catalytic activity was not pursued.
(46) Baker, M. V.; Field, L. D.; Hambley, T. W. Diamagnetic ↔ paramagnetic equilibria in solutions of bis(dialkylphosphino)ethane complexes of iron. *Inorg. Chem.* **1988**, *27* (16), 2872−2876.
(47) Baker, W.; Buggle, K. M.; McOmie, J. F. W.; Watkins, D. A. M. 718. Attempts to prepare new aromatic systems. Part VII. 15:16−Dihydro-15:16-diazapyrene. The synthesis of di(pyridine-2:6-dimethylene). *J. Chem. Soc.* **1958**, *0* (0), 3594−3603.
(48) Bottino, F.; Di Grazia, M.; Finocchiaro, P.; Fronczek, F. R.; Mamo, A.; Pappalardo, S. Reaction of tosylamide monosodium salt with bis(halomethyl) compounds: an easy entry to symmetrical N-tosyl aza macrocycles. *J. Org. Chem.* **1988**, *53* (15), 3521−3529.
(49) Boduszek, B.; Shine, H. J. Preparation of solid thianthrene cation radical tetrafluoroborate. *J. Org. Chem.* **1988**, *53* (21), 5142−5143.
(50) Che, C.-M.; Li, Z.-Y.; Wong, K.-Y.; Poon, C.-K.; Mak, T. C. W.; Peng, S.-M. A simple synthetic route to *N,N′*-dialkyl-2,11-diaza[3.3]-(2,6)-pyridinophanes. Crystal structures of *N,N′*-di-tert-butyl-2,11-diaza[3.3](2,6)pyridinophane and its copper(II) complex. *Polyhedron* **1994**, *13* (5), 771−776.
(51) Hassan, A. K.; Pardi, L. A.; Krzystek, J.; Sienkiewicz, A.; Goy, P.; Rohrer, M.; Brunel, L.-C. Ultrawide band multifrequency high-field EMR technique: a methodology for increasing spectroscopic information. *J. Magn. Reson.* **2000**, *142* (2), 300−312.
(52) Ozarowski, A. The Zero-Field-Splitting Parameter *D* in Binuclear Copper(II) Carboxylates Is Negative. *Inorg. Chem.* **2008**, *47* (21), 9760−9762.
(53) Abragam, A.; Bleaney, B. *Electron Paramagnetic Resonance of Transition Ions*; Oxford Classic Texts in the Physical Sciences; Oxford University Press: Oxford, U.K., 2012.
(54) Bendix, J. Ligfield. In *Comprehensive Coordination Chemistry II: From Biology to Nanotechnology, Vol. 2: Fundamentals: Physical Methods, Theoretical Analysis, and Case Studies*; Lever, A. B. P., Ed.; Elsevier: Amsterdam, 2003; Vol. 2, pp 673−676.
(55) Krzystek, J.; Swenson, D. C.; Zvyagin, S. A.; Smirnov, D.; Ozarowski, A.; Telser, J. Cobalt(II) "Scorpionate" Complexes as Models for Cobalt-Substituted Zinc Enzymes: Electronic Structure Investigation by High-Frequency and -Field Electron Paramagnetic Resonance Spectroscopy. *J. Am. Chem. Soc.* **2010**, *132* (14), 5241−5253.
(56) Frisch, M. J.; Trucks, G. W.; Schlegel, H. B.; Scuseria, G. E.; Robb, M. A.; Cheeseman, J. R.; Montgomery, Jr., J. A.; Vreven, T.; Kudin, K. N.; Burant, J. C.; Millam, J. M.; Iyengar, S. S.; Tomasi, J.; Barone, V.; Mennucci, B.; Cossi, M.; Scalmani, G.; Rega, N.; Petersson, G. A.; Nakatsuji, H.; Hada, M.; Ehara, M.; Toyota, K.; Fukuda, R.; Hasegawa, J.; Ishida, M.; Nakajima, T.; Honda, Y.; Kitao, O.; Nakai, H.; Klene, M.; Li, X.; Knox, J. E.; Hratchian, H. P.; Cross, J.

DOI: 10.1021/acs.inorgchem.7b02421
Inorg. Chem. 2017, 56, 14315−14325

B.; Bakken, V.; Adamo, C.; Jaramillo, J.; Gomperts, R.; Stratmann, R. E.; Yazyev, O.; Austin, A. J.; Cammi, R.; Pomelli, C.; Ochterski, J. W.; Ayala, P. Y.; Morokuma, K.; Voth, G. A.; Salvador, P.; Dannenberg, J. J.; Zakrzewski, V. G.; Dapprich, S.; Daniels, A. D.; Strain, M. C.; Farkas, O.; Malick, D. K.; Rabuck, A. D.; Raghavachari, K.; Foresman, J. B.; Ortiz, J. V.; Cui, Q.; Baboul, A. G.; Clifford, S.; Cioslowski, J.; Stefanov, B. B.; Liu, G.; Liashenko, A.; Piskorz, P.; Komaromi, I.; Martin, R. L.; Fox, D. J.; Keith, T.; Al-Laham, M. A.; Peng, C. Y.; Nanayakkara, A.; Challacombe, M.; Gill, P. M. W.; Johnson, B.; Chen, W.; Wong, M. W.; Gonzalez, C.; Pople, J. A. *Gaussian 09*, Revision D.01; Gaussian, Inc.: Wallingford, CT, 2013.

(57) Lee, C.; Yang, W.; Parr, R. G. Development of the Colle-Salvetti correlation-energy formula into a functional of the electron density. *Phys. Rev. B: Condens. Matter Mater. Phys.* **1988**, *37* (2), 785−789.

(58) Becke, A. D. Density-functional Thermochemistry. III. The Role of Exact Exchange. *J. Chem. Phys.* **1993**, *98* (7), 5648−5652.

(59) Stephens, P. J.; Devlin, F. J.; Chabalowski, C. F.; Frisch, M. J. Ab Initio Calculation of Vibrational Absorption and Circular Dichroism Spectra Using Density Functional Force Fields. *J. Phys. Chem.* **1994**, *98* (45), 11623−11627.

(60) Vosko, S. H.; Wilk, L.; Nusair, M. Accurate spin-dependent electron liquid correlation energies for local spin density calculations: a critical analysis. *Can. J. Phys.* **1980**, *58* (8), 1200−1211.

(61) Krishnan, R.; Binkley, J. S.; Seeger, R.; Pople, J. A. Self-consistent molecular orbital methods. XX. A basis set for correlated wave functions. *J. Chem. Phys.* **1980**, *72* (1), 650−654.

(62) McLean, A. D.; Chandler, G. S. Contracted Gaussian basis sets for molecular calculations. I. Second row atoms, Z = 11−18. *J. Chem. Phys.* **1980**, *72* (10), 5639−5648.

(63) Wachters, A. J. H. Gaussian Basis Set for Molecular Wavefunctions Containing Third-Row Atoms. *J. Chem. Phys.* **1970**, *52* (3), 1033−1036.

(64) Neese, F. *ORCA—an Ab Initio, Density Functional and Semiempirical Program Package*, Version 3.0.3; Max Planck Institut für Chemische Energiekonversion: Mülheim an der Ruhr, Germany, 2014.

(65) Neese, F. The ORCA program system. *Wiley Interdiscip. Rev.: Comput. Mol. Sci.* **2012**, *2* (1), 73−78.

DOI: 10.1021/acs.inorgchem.7b02421
Inorg. Chem. 2017, 56, 14315−14325